S.I. : ADJACENT INTERACTING MASONRY STRUCTURES

Simulation of blind pre-diction and post-diction shaking table tests on a masonry building aggregate using a continuum modelling approach

Abide Aşıkoğlu[1] · **Jennifer D'Anna[1]** · **Rafael Ramirez[1]** · **Fabio Solarino[1]** ·
Antonio Romanazzi[1] · **Maria Pia Ciocci[1]** · **Nicoletta Bianchini[1]**

Abstract

Masonry buildings of historical centres are usually organized within aggregates, whose structural performance against seismic actions is challenging to predict and constitutes still an open issue. The SERA—AIMS (Seismic Testing of Adjacent Interacting Masonry Structures) project was developed to provide additional experimental data by testing a half-scale, two-unit stone masonry aggregate subjected to two horizontal components of dynamic excitation. In this context, this paper investigates the reliability of the modelling approach and the assumptions adopted to generate a three-dimensional continuum finite element model. The work involves two stages, namely a blind pre-diction and a post-diction phase, and proposes a series of simulation analyses including a strategy to shorten the actual records and save computation costs. The study was performed to investigate the extent of uncertainty in modelling for such masonry aggregates in relation to the experimental outcomes. Pre-diction results were proven to be not accurate in terms of predicted displacements and damage patterns. The upgrades introduced for the post-diction analyses, including the calibration of the elastic modulus and the introduction of a non-linear interface between the two units, allowed to improve the outcomes, with reasonable results in terms of predicted base shear force, displacements along Y-direction and damage pattern for the non-linear stage. The overall approach showed to be appropriate for the structural analysis of existing masonry aggregates, but the accurate modelling of this type of structure remains challenging due to the high level of uncertainties.

Keywords Stone masonry aggregate · Non-linear dynamic analysis · Historical structures · Finite element modelling · Shaking table test · Numerical simulation

✉ Rafael Ramirez
    rafael.alvarezdelara@gmail.com

[1] Department of Civil Engineering, ISISE, University of Minho, 4800-058 Azurém, Guimarães, Portugal

Ⓐ Springer

1 Introduction

Since the early 1970s, scientific research has developed a strong interest in the seismic risk assessment of masonry buildings that make up most of the historical city centres. As a result, several technical documents and papers have been produced. The majority of these works are concerned with the identification of procedures for understanding the structural system. Moreover, the technical documents focus on the definition of building typologies and the assessment of seismic vulnerability by adopting different methodologies.

The current Italian technical standard (NTC 2018) defines the masonry buildings in a historical centre as Structural Units (SUs) which form Structural Aggregates (SAs) and provide general indications on how to analyse this type of construction. The code recognizes the unsuitability of applying assessment techniques usually used for new buildings for the study of masonry aggregates; however, the standard lacks providing alternative resolution methods. For the analysis of a historical centre, it specifies that the SU should be identified within the SA, highlighting the actions that can be derived from adjacent SUs. Moreover, it notes that the effects of the connections between SUs on the global performance of the SA should be accounted for. Other technical standards, such as the Eurocode for the "Design of structures for earthquake resistance—Part 3: Strengthening and repair of buildings" (Eurocode 8 2005) and the American Standard for the "Seismic Evaluation and Retrofit of Existing Buildings" (ASCE 2014), do not provide any specific indication about aggregated buildings in historical centres.

The lack of consistent procedures and specific technical standards for the analysis of this construction typology is related to the uniqueness that characterizes each historical centre, which does not allow the development of mandatory rules of general application. Several guidelines and specialized books have been published as a result of studies performed in different old city centres. In particular, some works compare the analyses done before and after the occurrence of seismic events and point out the outcomes achieved by using different retrofitting techniques (Giuffré 1990; Giuffrè et al. 1993; Milano et al. 2006; Carocci et al. 2009; De Sortis et al. 2009; DPCM 2011; DPC 2012; Mochi and Predari 2016; Lombardo et al. 2018). Moreover, these documents provide a thorough review of the procedures necessary for the assessment of building systems in historical city centres.

As an example, the Italian code NTC (2018) proposes a detailed methodology to collect and analyse relevant data necessary before any intervention on existing buildings. First, a comprehensive identification of the construction and modification stages of the investigated building must be performed (Fig. 1). In the case of building aggregates,

Fig. 1 Aggregate buildings: **a** evolution by the individuation of different SUs (adapted from Giuffré 1990); **b** geometrical survey of buildings in aggregates

they must be analysed in their specific urban and environmental setting as well. The identification of construction techniques and the morphological changes of the structures must be examined to attain a better understanding of their historical evolution. In particular, the superposition of different materials and building technologies helps to define hypotheses on the original condition and subsequent evolution of the aggregates. Finally, these hypotheses will be confirmed through the survey of the building geometry and the construction system, the detection of damage and crack patterns, and the mechanical characterization of the materials.

In the current scientific literature, several methods can be found for the vulnerability assessment of masonry buildings in historical city centres, based on a multi-level approach characterized by increasing knowledge and in-depth in-situ evaluations (Cattari et al. 2006). With the improvement of structural analysis and design software, nonlinear analyses are used to better describe the seismic performance of different types of structures. These analyses can be generally categorized into two groups, namely Non-Linear Time History Analysis (NLTHA) and Non-Linear Static or Pushover Analysis (NLSA/POA), and several studies have been performed based on these approaches, e.g. Fragiadakis and Vamvatsikos (2010), Mendes (2012), Lourenço et al. (2013), Zacharenaki et al. (2013), Liu and Kuang (2017), Aşıkoğlu et al. (2020, 2021). The basic requirement of every modelling technique and approach is to adequately describe the geometry, morphology, connections, and support conditions, which is surely a challenging achievement. Another challenge is related to the lack of clear modelling guidelines and standards for SAs in historical centres, which results in considerable uncertainties in representing the interaction between adjacent units, especially concerning the connection system between SUs.

Advances in the development of analysis methods for such aggregates have been impeded by the lack of experimental data, due to the high costs and the complexity of performing tests on large-scale aggregates. To contribute to the state of the art on the seismic behaviour of aggregates, the Adjacent Research Infrastructure Alliance for Europe (AIMS) project from the Seismology and Earthquakes Engineering Research Infrastructure Alliance for Europe (SERA) provided experimental data by testing an aggregate of two half-scale stone masonry buildings under two horizontal components of dynamic excitation. A blind pre-diction competition was organized before the test; later, participants were provided with the actual seismic input and relevant test data to run post-diction analyses. In this context, the present paper aims at comparing the results of a three-dimensional continuum finite element model with the outcomes obtained from the experimental test. The simulation results obtained during the prediction stage are first compared to the experimental outputs to point out the weaknesses of the adopted modelling strategy. This stage is crucial to understand the improvements required for the considered modelling approach. During the post-diction phase, the numerical model is updated and calibrated based on the experimental data.

2 Description of the experimental campaign

This section provides an overview of the experimental campaign carried out by Tomić et al. (2022). First, the geometric properties of the prototype building are presented, and, followed by the procedure adopted for the shaking table testing is described.

2.1 Geometry of the prototype building

The test specimen was a half-scale prototype of a masonry aggregate, composed of two units. Unit 2 consisted of two floors and a total height of 3.15 m; it had a square shape with four walls and a dimension of 2.5 m × 2.5 m. Unit 1 consisted of one floor with a height of 2.2 m. Unit 1 had a U-shape with three walls and dimensions of 2.5 m × 2.45 m. The dimensions of the floor plan with beams and façades are reported in Fig. 2. The wall thickness was equal to 300 mm for Unit 1, and 350 mm and 250 mm for Unit 2 on the first and the second floor, respectively. Spandrels under the openings had a thickness of 15 cm. There was no interlocking between the two units and the connection consisted of a single mortar layer. The horizontal elements consisted of floor diaphragms with 8 cm × 16 cm timber beams and 2 cm thick timber planks perpendicular to the beams. These diaphragms had different orientations, with Unit 1 beams parallel to the X-direction and Unit 2 beams along the Y-direction.

2.2 Seismic input and loading protocol

First of all, it should be underlined that the actual testing sequence differed from the original plan. Thus, instead of a total of twelve steps (two uni-directional tests plus one bi-directional test, for four intensity levels), as reported in Table 1, only ten steps were involved in the testing sequence (Tomić et al. 2022), see Table 2. Due to this discrepancy, Table 2 shows the experimental outputs compared to blind pre-diction results to account for differences between nominal and effective shaking table accelerations. Comparing the effective and nominal shaking table accelerations in terms of acceleration spectra, it was found that for the period range close to the fundamental periods, the demand imposed in Run 2.1 (experimental) closely corresponds to the nominal demand planned for Run 3.1 (Level III—75%) (Tomić et al. 2022). Thus, the predictions of Run 3.1 are here compared to the experimental results of Run 2.1, which was the last run before strengthening measures were applied. Run 2.1 and 3.1 are uni-directional tests in Y-direction. Considering the X-direction, the prediction of Run 3.2 (Level III—75%) is here compared to the experimental results of Run 2.2S (experimental), for the
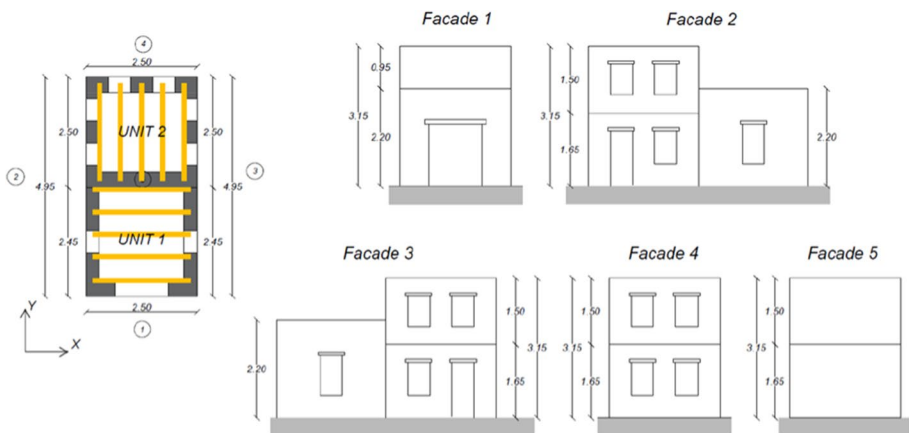

Fig. 2 SERA AIMS test specimen floor plan with beam orientation and façade layout of the two units (Tomić et al. 2022)

Table 1 Nominal shaking table testing sequence (Tomić et al. 2022)

Run number	Run notation	Direction	Level of shaking (shaking table capacity) (%)	Nominal PGA (g)
1	1.1	Y	25	0.219
2	1.2	X	25	0.156
3	1.3	Bidirectional	25	0.219(Y)/0.156(X)
4	2.1	Y	50	0.438
5	2.2	X	50	0.313
6	2.3	Bidirectional	50	0.438(Y)/0.313(X)
7	3.1	Y	75	0.656
8	3.2	X	75	0.469
9	3.3	Bidirectional	75	0.656(Y)/0.469(X)
10	4.1	Y	100	0.875
11	4.2	X	100	0.625
12	4.3	Bidirectional	100	0.875(Y)/0.625(X)

Table 2 Actual applied testing sequence of the shaking table test (Tomić et al. 2022)

Run number	Run notation	Direction	Level of shaking (shaking table capacity) (%)	Nominal PGA	Effective PGA
1	0.1	Y	12.5	0.110	0.113
2	0.2	X	12.5	0.078	0.075
3	0.3	Bidirectional	12.5	0.110(Y)/0.078(X)	0.114(Y)/0.072(X)
4	1.1	Y	25	2250.219	0.170
5	1.2	X	25	0.156	0.178
6	1.3	Bidirectional	25	0.219(Y)/0.156(X)	0.208(Y)/0.174(X)
7	2.1	Y	50	0.438	0.593
8	2.1S	Y	50	0.438	0.615
9	1.2S	X	25	0.156	0.258
10	2.2S	X	50	0.313	0.425

same reasons mentioned for Y-direction. In Run 2.2S the test specimen was already strengthened. Thus, the comparison between numerical and experimental results is affected by some factors, namely the discrepancies between the nominal and the effective testing sequence, the discrepancies between the nominal and effective shaking table acceleration and, for the X-direction, a discrepancy in the model since the test specimen was strengthened and the numerical model was unstrengthened.

3 Blind pre-diction analysis: model description and results

In this section, the characteristics of the case-study aggregate are discussed. In particular, the geometrical arrangement, the modelling approach, and the material properties included in the model are presented.

3.1 Numerical modelling approach and materials

The structure was analysed through a macro-modelling approach (Lourenço and Ramos 2004) to generate a 3D Finite Element (FE) model in DIANA FEA (2022). The numerical model and the discretization of the mesh were a compromise between accuracy and computational effort, taking into account the number of nodes and elements across the thickness of the walls. Thus, the mesh was formed by regular hexahedra with a size of 50 mm, and the model was composed of eight-node isoparametric solid brick elements (HX24L). Overall, there were 81,384 elements and 100,803 nodes, which defined more than 300,000 degrees of freedom (Fig. 3).

Regarding the wall-to-wall connections, no specific contact or interface element was adopted between orthogonal walls and, therefore, they were modelled as a continuum. On the other hand, the shared elements of the two units were disconnected which simulates no connection between the coincident source and target geometries in DIANA. In this way, it was possible to split a shared node of two adjacent elements into two separate nodes. Interface elements between the two units were avoided due to the lack of information about the required stiffnesses. Preliminary analyses, namely structural linear static and eigenvalue analyses were performed to test the validity of the approach adopted for the connection between the units. As expected, it was verified that the split nodes had independent behaviour.

The possible diaphragmatic behaviour of the timber deck was neglected and, therefore, the floor was not modelled. On the other hand, considering the intended weak connection between the timber beams and the walls, the beams were not included. The self-weight of the deck and beams as well as the additional weight on the floors of Unit 2 were redistributed on the walls. In particular, the non-modelled masses were applied at the locations corresponding to the head of the beams, introduced as a masonry material with equivalent density (Fig. 4a). Regarding the boundary conditions, the model was considered fully fixed at the base (Fig. 4b).

The timber lintels were modelled with an elastic isotropic behaviour and properties assumed for typical timber (CEN 2009). The constitutive behaviour of the masonry material was defined by a Total Strain Rotating Crack Model (Lourenço 1996). In this model, stress and strain relationships are defined along the principal directions of the strain vector.

Fig. 3 **a** North–West and **b** North–East views of the meshed 3D FE model
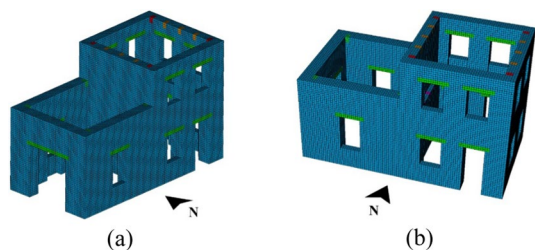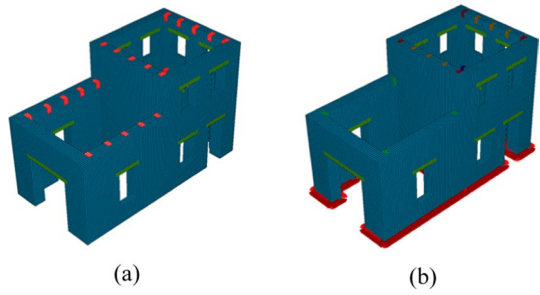
(a)   (b)

Fig. 4 3D FE model: **a** application of non-modelled masses; **b** boundary conditions at the base of the model

(a)   (b)

The material cracks when the maximum principal stress exceeds the tensile strength, and the orientation of the cracking remains orthogonal to the maximum principal strain. Therefore, the direction of the cracks is updated accordingly. A variety of studies have demonstrated that rotation cracks behave realistically as opposed to fixed cracks, which tend to show a stiffer behaviour and cause an increase in stress for shear-controlled mechanisms in URM buildings (Rots 1988). Moreover, only the physical nonlinearity was considered, whereas the geometrical nonlinearity was neglected since the stability problem was not expected (Imai and Frangopol 2000). The constitutive model was based on an exponential stress–strain relation under tension, whereas in compression a parabolic relation for both hardening and softening was adopted (Fig. 5). The material properties were calibrated according to the available experimental tests (uniaxial tests and in-plane compression-shear tests) (Senaldi et al. 2018). Based on the range of material properties found in the Italian code (Circolare NTC 2018, and NTC 2018), the elastic modulus was changed from the value of 3.4 GPa (provided for blind pre-diction) to the value of 2.0 GPa, representing an approximation of the characteristics for masonry with regular soft stones. The main reason for such a decision was the fact that the model with Young's modulus of 3.4 GPa resulted in extremely low deformations. Therefore, it was decided to adopt the lower bound limit suggested by the Italian code for this type of masonry wall. The material properties used for the pre-diction model are collected in Table 3.

Regarding the damping model, the Rayleigh damping coefficients a and b were defined according to (Chopra 2012) as given in Eq. (1). Consequently, the considered frequencies were $f_1 = 15.07[Hz]$ and $f_2 = 192.39[Hz]$, which were related to the first eigenvalue and the eigenvalue for which 90% of the cumulative modal mass was reached. Additionally, a damping ratio $\xi = 3\%$ was assumed according to Mendes and Lourenço (2014) as a starting
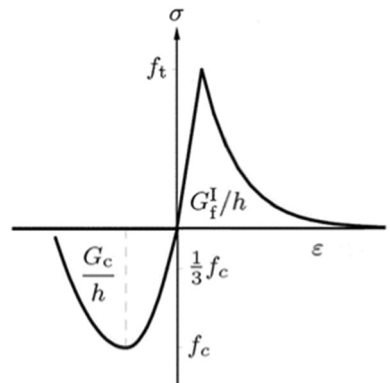
Fig. 5 Constitutive law of masonry (DIANA FEA 2022)

Table 3 Material properties adopted in the numerical model

| | Masonry | Timber |
	Parabolic and exponential diagrams	Elastic isotropic
Elastic modulus (GPa)	2.00	13.00
Specific weight (kg/m^3)	1980	750
Poisson ratio (–)	0.14	0.3
Compressive strength (MPa)	1.30	–
Compressive fracture energy (kN/m)	2.670	–
Tensile/Yield strength (MPa)	0.17	–
Tensile fracture energy (kN/m)	0.012	–

point. It is noted that a sensitivity study for the value of the damping ratio was performed in the post-diction phase so that the results were compared with the experimental ones (See Sect. 4.3.2).

$$a = \xi \cdot \frac{(2\omega_1\omega_2)}{(\omega_1 + \omega_2)} \text{ and } b = \xi \cdot \frac{2}{(\omega_1 + \omega_2)} \tag{1}$$

where $\omega_1 = 2\pi \cdot f_1$ and $\omega_2 = 2\pi \cdot f_2$ in [rad/s].

Once the model characteristics were defined, non-linear time-history analyses were performed. The model was subjected to one- and two-component excitations, using the two horizontal components of the 1979 Montenegro earthquake from Albatros station. The maximum accelerations that could be applied to the test specimen by the shaking table were 0.875 g along the Y-direction and 0.625 g along the X-direction; thus, these reference values were also considered for the numerical analyses. The theoretical specified limits were required to be reached in four steps, namely by applying the ground motion at 25%, 50%, 75%, and 100% of those limits. Each level involved three stages, namely a uni-directional test in Y-direction, a uni-directional test in the X-direction, and a bi-directional test with X- and Y-components.

3.2 Comparison with the experimental results

The current section is dedicated to the comparison between the results obtained from the pre-diction analyses and the experimental outputs. It is noted that the model with Young's modulus of 2.0 GPa moves significantly less than the experimental results (min 70%, max 98%) within the linear range (Run 2.3). The comparison is made in terms of displacements at the roof level, interface openings, and base-shear forces. Based on the available experimental results, Table 4 reports the parameters considered for the comparison between the experimental test and numerical analyses, for Run 2.3, 3.1, and Run 3.2 of the blind pre-diction. In particular, these parameters include the maximum absolute values of the recorded relative displacements of the units with the ground (Rd1-6), the interface openings (Id1-4), and the base shear values (BSy, BSx). The points where displacements and interface openings were recorded are presented in Fig. 6. Based on the available experimental results, the outputs of the FE analyses are commented regarding Rd2, Rd3, Id3, Id4, BSx, and BSy values, for Run 3.1 and

Table 4 Experimental outputs compared with blind pre-diction results

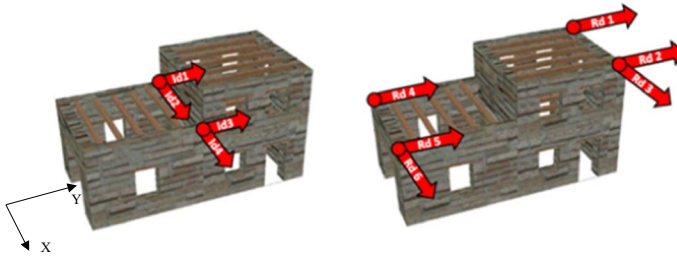| Experimental run	Blind pre-diction	Parameters compared
1.3	2.3	BSy, Rd2, Id3
		BSx, Rd3, Id4
2.1	3.1	BSy, Rd2, Id3
2.2S	3.2	BSx, Rd3, Id4

Fig. 6 Displacements relative to the ground (Rd1-6) and interface openings (Id1-4)

Table 5 Comparison between experimental and blind-prediction results in terms of displacements at roof level (Rd), interface openings (Id), and base-shear values (BS)

Run notation	Step and direction	Quantities compared	Experimental result	Numerical result	Difference %
2.3	50% in Y-direction	Rd2	4.67 mm	0.58 mm	− 88
		Id3	4.07 mm	0.08 mm	− 98
		BSy	60 kN	107 kN	+ 78
	50% in X-direction	Rd3	3.83 mm	0.58 mm	− 85
		Id4	4.88 mm	1.46 mm	− 70
		BSx	62 kN	82 kN	+ 32
3.1	75% in Y-direction	Rd2	60 mm	2.50 mm	− 96
		Id3	20 mm	0.18 mm	− 99
		BSy	180 kN	155 kN	− 14
3.2	75% in X-direction	Rd3	23 mm	1.00 mm	− 96
		Id4	8 mm	3.14 mm	− 61
		BSx	85 kN	108 kN	+ 27

3.2 (blind pre-diction runs, see Table 4). The comparison between experimental and pre-diction is shown in Table 5. Furthermore, a qualitative comparison is carried out between the predicted damage mechanisms and the ones recorded during the experimental campaign. In particular, the damage mechanisms reported after Level 3 (75% shaking table capacity) are here discussed, since they were the closest match to the actual Runs 2.1 and 2.2S in terms of the spectrum response and PGA.
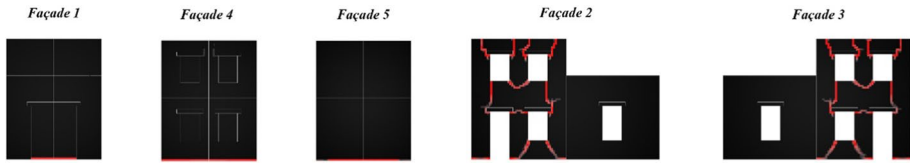
Fig. 7 Principal tensile strain distribution (max 0.01) obtained for 75% shaking table capacity, considering the Y-component
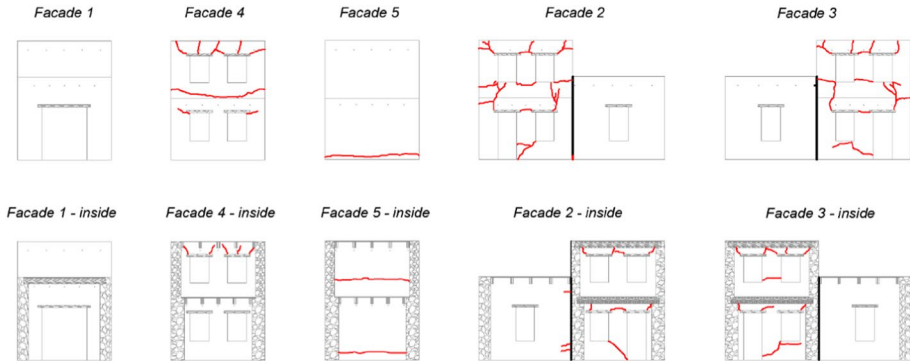

Fig. 8 Crack map at the end of Run 2.1 (Tomić et al. 2022)

3.2.1 Results at the end of run 3.1 (75% in Y-direction)

Considering the peak roof displacements for Run 3.1 (75% in the Y-direction), the obtained FE result for Rd2 is equal to 2.50 mm (96% less), while the corresponding experimental value is about 60 mm. Considering the interface opening Id3 for Run 3.1, the FE analysis provided a value of 0.18 mm, while the experimental value was equal to 20 mm. Recalling the base-shear results, the FE values obtained by performing analysis along Y-direction (BSy) for Run 3.1 was 155 kN with an error of 14%; the corresponding experimental value was nearly 180 kN.

Figure 7 reports the damage in the FE model for 75% shaking table capacity along the Y-direction (Run 3.1 of the blind pre-diction) and Fig. 8 presents the crack map for the tested aggregate at the end of the experimental Run 2.1. The maximum value for the principal tensile strain is selected as 0.01 according to Mendes (2014). The comparison shows well-replicated damage mechanisms in Façades 2 and Façade 3 of Unit 2, with the formation of flexural cracks. Regarding Façade 4, the numerical model shows signs of flexural cracks like those recorded in the test model, which is characterized also by a horizontal crack at the spandrel between openings. No damage was detected in Façade 5 for the numerical model; only a horizontal crack appeared at the bottom of the experimental model. At this stage, Unit 1 did not develop any damage.

3.2.2 Results at the end of run 3.2 (75% in X-direction)

The peak of the roof displacement Rd3 for Run 3.2 (75% in the X-direction) obtained from FE analysis is equal to 1.00 mm, while the experimental value is equal to 23 mm.
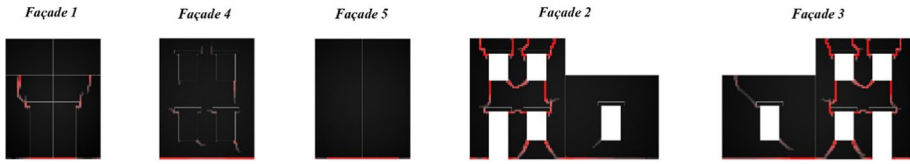
Fig. 9 Principal tensile strain distribution (max 0.01) obtained for 75% shaking table capacity, considering the X-component
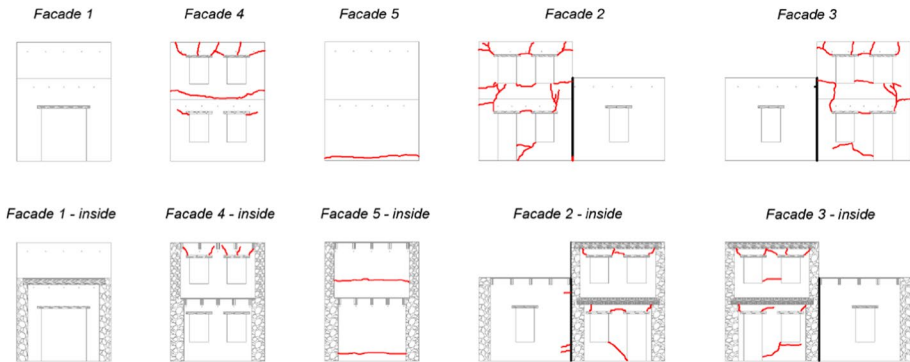

Fig. 10 Crack map at the end of the Run 2.2S (Tomić et al. 2022)

Referring to the interface opening Id4 for Run 3.2, the FE analysis provided a value of 3.14 mm, while the experimental value was equal to 8 mm. Considering the BSx, the simulation value obtained for Run 3.2 was equal to 108 kN and the corresponding experimental value was equal to 85 kN. Thus, the pre-diction model showed lower displacements and interface openings compared to the experimental outputs. These results point out that the stiffness of the aggregate was overestimated.

Figure 9 represents the damage of the FE model for 75% shaking table capacity along the X-direction (Run 3.2 of the blind pre-diction), whereas Fig. 10 presents the crack map for the tested aggregate at the end of the experimental Run 2.2S. At this stage, for both the test and the FE models, Unit 1 starts to show crack propagation, with flexural cracks in the spandrel of Façade 1. Moreover, Façade 2 and Façade 3 (Unit 1) of the numerical model show few shear cracks in the out-of-plane direction, probably due to the lack of connection between the two units; these cracks were not recorded in the experimental model, which shows instead horizontal cracks at the bottom of Unit 1. As for Unit 2, Façade 2 and Façade 3 of the numerical model do not show the appearance of new cracks, coherently with the experimental model. Shear cracks appeared at the spandrel between the openings of Façade 4 of the test model, while the same façade of the FE model shows some flexural and shear cracks at the corners of the top and bottom openings respectively. Regarding Façade 5, the numerical model still does not show any damage, whereas the test model presents some shear cracks.

### 3.2.3 Results at the end of run 3.3 (75% bidirectional)

Figure 11 reports the crack propagation of the FE model obtained for 75% shaking table capacity, considering bi-directional input with the X- and Y-component. The corresponding test was not performed experimentally. The image shows the evolution of the previously developed damage and the appearance of new cracks. In particular, several shear cracks developed in the spandrels between the openings in Façade 2 and Façade 3 of Unit 2. At this stage, Façade 4 of the same unit is subjected to severe flexural and shear cracks, similar to those recorded in the test model during previous stages. Moreover, Façade 4 underwent an important out-of-plane movement of the central upper part, underlining the local behaviour of the wall. Horizontal and flexural cracks appeared in Façade 5, which replicate quite well the ones registered during experimental tests performed for Y-component and X-component.

3.2.4 Lessons learned from the blind prediction model

At the end of the experimental Run 1.3 (blind pre-diction 25% bi-directional), a separation between the two structural units within the aggregate was observed. This phenomenon could not be detected in the numerical model because of the disconnected elements, which did not take into account the possible interaction between the two units.

According to the previous comparison between experimental and blind pre-diction results, it seems clear that a series of upgrades should be introduced to improve the numerical response of the model. In particular, the following aspects need to be considered. First, the blind pre-diction model was not able to capture the interaction between the two aggregate units because of the use of disconnected elements. Hence, the introduction of an interface between Unit 1 and Unit 2 seems necessary. Secondly, the numerical model showed a local out-of-plane behaviour of Façade 5 that was not recorded in the experimental model,

Fig. 11 Principal tensile strain distribution obtained for 75% shaking table capacity, considering bi-directional input with the X- and Y-components
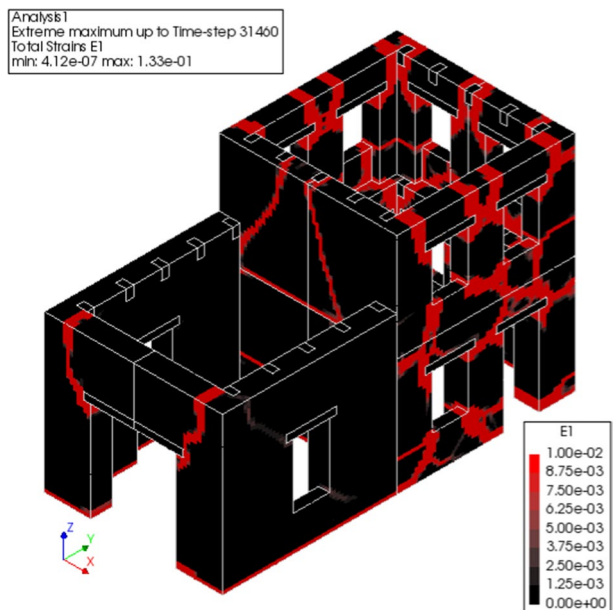
pointing out the need to introduce some updates to guarantee a more global behaviour. Finally, the numerical results underestimated the displacement demands, most likely due to an overestimated stiffness of the model, which can be related to the assumption of the boundary conditions (fixed support) and/or the considered value for the elastic modulus. In this context, it was decided to calibrate the elastic modulus to match the experimental response since it is a more straightforward approach compared to the introduction of new boundary conditions.

4 Post-diction analysis: model updating and results

Based on the comparison of the experimental results and blind pre-diction analysis, a set of upgrades was considered to improve the numerical simulation. The following methodology for model updating is adopted: (a) introduction of an interface between Unit 1 and Unit 2; (b) introduction of tying elements; and (c) calibration of the elastic modulus. Briefly, interface elements were implemented between the two units to simulate their interaction. Moreover, tying elements were selected as a tool to obtain more accurate damage mechanisms. Lastly, model calibration through the elastic modulus was carried out to match the experimental displacements. To reduce the computational cost, it was decided to apply the dynamic inputs of Run 1.3 and Run 2.1 as two independent analyses. The main reason for such a decision is that there is no evidence of damage until Run 1.3. On the other hand, due to the limitations of the chosen software, it was not possible to incorporate the strengthening into the already damaged model after Run 2.1. Therefore, Run 1.3 was used to calibrate the numerical model within the linear range, whereas Run 2.1 was utilized to study the non-linear behaviour before the strengthening.

4.1 Introduction of an interface between Unit 1 and Unit 2

A mesh set of interface elements was introduced between Unit 1 and Unit 2 to simulate the detachment of the masonry aggregates that is observed at the end of Run 1.3 (Fig. 12) and the possible pounding effect. The disconnection of the two units that were employed for the prediction phase did not allow for to capture of the experimentally observed interaction between the aggregates. In order to obtain a more accurate behaviour, the contact between the units was modelled through non-linear interface elements in the updated model. In particular, CQ48I
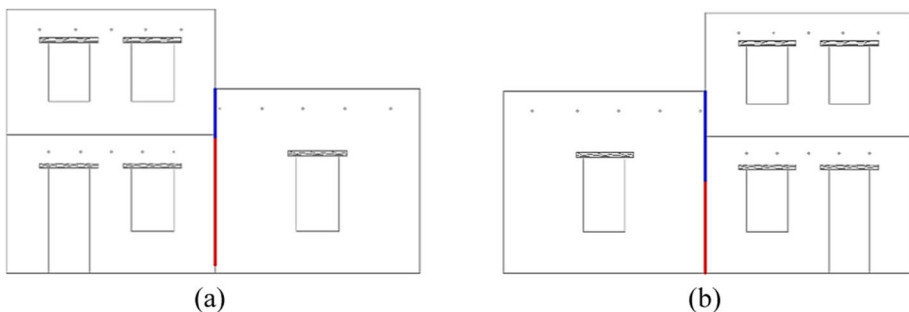

(a)   (b)

Fig. 12 Damage distribution after Run 1.1 (blue) and 1.3 (red): **a** Façade 2; **b** Façade 3

elements were used, that is second-order plane quadrilateral elements working as an interface between two planes in a three-dimensional configuration, as shown in Fig. 13.

The normal stiffness modulus was calculated considering the elastic modulus of masonry and the length of the longitudinal walls of Unit 1, such as:

$$K_n = \frac{E}{L} \left[\text{kN/m}^3\right] \tag{2}$$

This formulation is derived from the definition of the spring constant, k [kN/m], which can be calculated from the stress–strain relationship, $\sigma = E \cdot \varepsilon$, alternatively expressed as:

$$\frac{F}{A} = E \cdot \frac{\Delta L}{L} \tag{3}$$

which can be rearranged as:

$$F = \frac{A \cdot E}{L} \Delta L \tag{4}$$

Moreover, the spring equation (Hooke's law) yields:

$$F = k \cdot \Delta L \tag{5}$$

Thus, the spring constant can be calculated by relating Eqs. (4) and (5):

$$k = \frac{A \cdot E}{L} \tag{6}$$

The spring equation can also be expressed with respect to the area, such as:

$$\frac{F}{A} = \frac{k}{A} \cdot \Delta L = K \cdot \Delta L \tag{7}$$
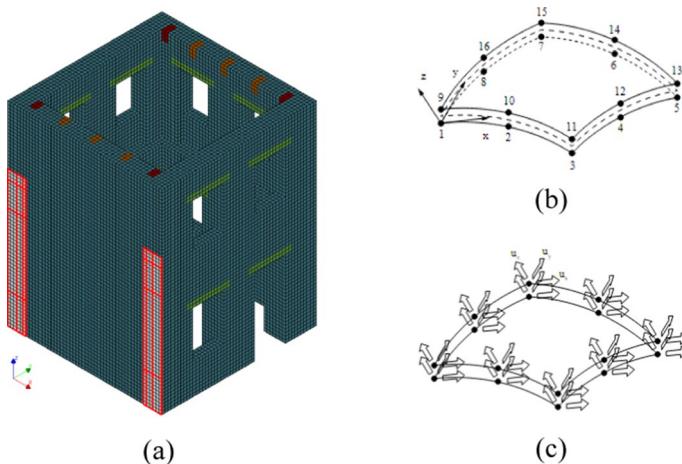
Fig. 13 Interface elements CQ48I: **a** mesh set (illustrated in red); **b** topology; **c** displacements (DIANA FEA 2022)

Fig. 14 Elastic non-linear behaviour of the interface between the aggregate units
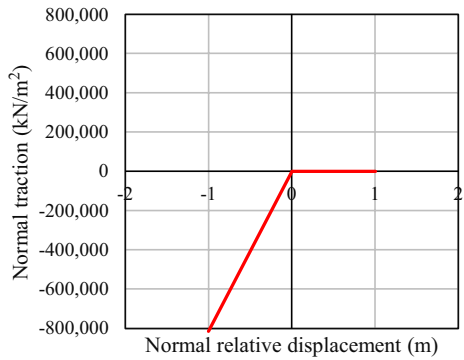
where K [kN/m^3] represents the stiffness modulus. Therefore, by rearranging terms and relating to the stress–strain relationship:

$$K = \frac{F}{A \cdot \Delta L} = \frac{E}{L} \tag{8}$$

Note that the same analogy can be achieved by relating Eqs. (3) and (7).

Considering the lack of a dynamic identification to calibrate the Young's modulus and effective wall length accounting for openings, and after running a few alternative scenarios, it was decided to fix the interface stiffness as $K_n = 8.16 \cdot 10^5$ kN/m^3. Note that this corresponds to a Young's modulus of 2.0 GPa. This approach allowed concentrating the subsequent calibration process solely on the Young's modulus of masonry (see Sect. 4.3.1). In turn, the transversal stiffness modulus was assumed 40% of the normal value, thus $K_t = 3.27 \cdot 10^5$ kN/m^3. The non-linear behaviour was defined utilizing a relative displacement-traction diagram. The curve was defined so that the slope in compression equals K_n, whereas the slope of the tensile component is reduced to 1% K_n (Fig. 14). To guarantee numerical stability, the transition between the two stages must be smooth and avoid the origin, that is, the zero-displacement zero-traction point in the diagram where the normal relative displacement and normal traction are equal to zero.

4.2 Introduction of tying elements

The blind pre-diction model revealed certain damage distributions that the experimental model did not experience. To overcome the unexpected crack pattern, three groups of tying elements were introduced in the post-diction model, as highlighted in yellow in Fig. 15. Tying elements are linear dependences between nodal variables and can be linked via one-to-one or one-to-many connections. They are mainly specified through master and slave nodes. For instance, Façade 5 of Unit 2 depicted no damage while the blind pre-diction model showed out-of-plane mechanisms and cracks. This might be due to the lack of diaphragmatic action in the numerical model resulting in the local response. The first group of tying elements connects the roof-level beams of Unit 2, imposing the same displacement at the opposite façades in the longitudinal direction. Therefore, the out-of-plane response of Façade 5 is prevented, and relatively more global behaviour is ensured. Still, the numerical model can experience different displacements along the façade at the roof level.

The second group of tying elements was defined for the window openings in the second level of Unit 2 in order to improve the stiffness of the spandrel units. In particular, the
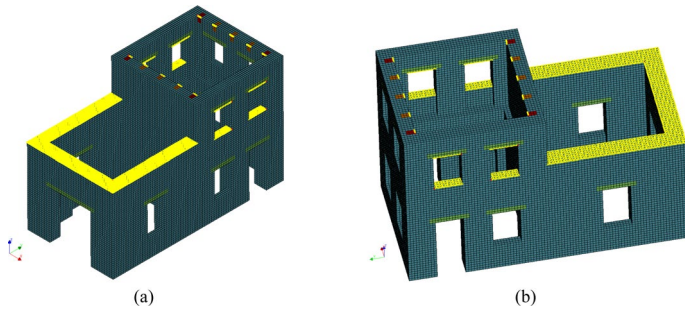
Fig. 15 Tying elements implemented in the updated numerical model, **a** view 1, **b** view 2

displacements in the vertical direction were assumed to be the same, as shown in Fig. 16. Moreover, each set of tying elements was defined individually as depicted in different colours in Fig. 16b. In the blind pre-diction model, it was observed that shear cracks were spreading through the spandrels, which might be the result of a lack of in-plane resistance. With the help of tying elements, the boundary conditions of the spandrels above and below the windows were updated and rotation degrees of freedom were removed.

As discussed previously, the blind pre-diction model exhibited moderate out-of-plane damage in Unit 1 whereas there was no evidence of local behaviour governing the response in the experimental campaign. Accordingly, the third group of tying elements were implemented for the post-diction model. These tying elements were applied at the roof level to ensure equal displacements in the longitudinal (Y) direction and prevent the out-of-plane mechanism. Thus, two independent sets of tying were introduced, namely one for Unit 1 and another one at the roof level of Unit 2.

4.3 Calibration of the numerical model

To construct a representative numerical model, a calibration procedure is necessary. In general, numerical models are calibrated based on the ambient vibration measurements with good accuracy (Mendes 2012; Lourenço et al. 2013; Aşıkoğlu et al. 2019; Bianchini et al. 2020, 2022). However, within the blind pre-diction competition context, the ambient vibration measurements were not available for the participants and therefore, due to the lack of data, the authors were not able to implement this approach.
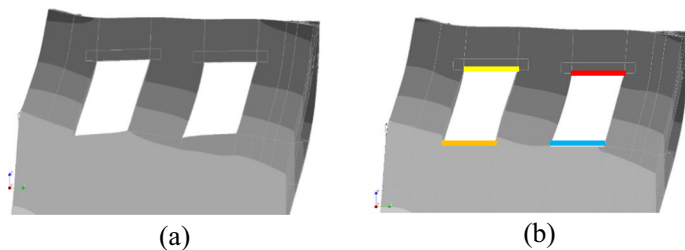

Fig. 16 Deformed shape of Unit 2 second floor (scale factor 0.1): **a** without tying elements; **b** with tying elements in the window openings
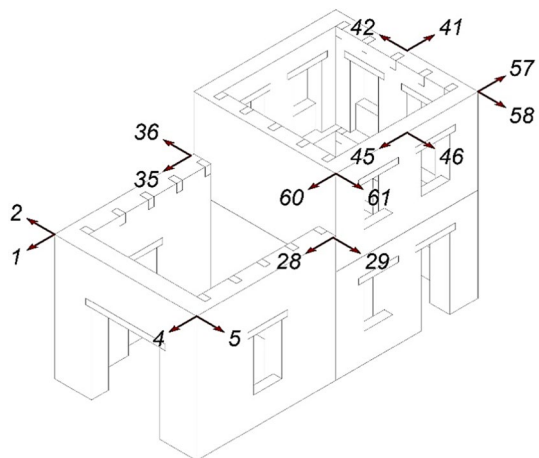
4.3.1 Young's modulus

As discussed in Sect. 3, a value of 2.0 GPa for the Young's modulus of masonry led to a response in which the structure was too stiff and the level of deformations was significantly low in comparison to the experimental values. Due to the lack of information on the dynamic properties of the experimental structure, it was decided to calibrate the elastic modulus of masonry by matching the maximum displacements at Run 1.3, when the specimen was still in the elastic range (no damage). Figure 17 depicts the location of the control points that are compared in the displacement comparison figures.

In particular, the maximum displacement of Unit 2 at the roof level was taken as a reference for calibration. The obtained experimental displacement was about 4.5 mm. For the calibration process, the Young's modulus of masonry was changed until a comparable displacement value was achieved. Following a sensitivity analysis procedure, gradually decreasing values of the Young's modulus were tested, namely 1000 MPa, 500 MPa, and 160 MPa (Fig. 18). As expected, lower Young's moduli resulted in higher maximum displacements. Note that the displacements obtained with Young's moduli 1000 MPa and 500 MPa are below 1.0 mm for all cases. Conversely, the Young's modulus of 160 MPa shows significant improvements, especially for Unit 2 in the Y-direction. Nevertheless, the maximum displacement lay behind the target experimental value for the rest of the cases. It is noted that this value is about 20 times lower than the value obtained from material characterization tests carried out by Senaldi et al. (2018). Such a low value is considered an acceptable compromise for the present study, but it should not be applied systematically to other similar cases, for which a sensitivity analysis should be performed as well.

Accordingly, an eigenvalue analysis was performed. The modal properties and mode shapes for the first four modes are presented in Table 6 and Fig. 19. Nearly 41% of the mass participates in the transversal (X) direction with a frequency of 5.7 Hz, whereas the mass participation ratio in the longitudinal (Y) direction is 60.85% with a frequency of 6.3 Hz. The first mode is mainly translational and localized in Unit 2 in the transversal direction. Conversely, mode 2 is mainly translational and governs both units in the longitudinal (Y) direction. The third mode is a local mode concentrated on Unit 1 with slight interaction with Unit 2 in the transversal (X) direction. Lastly, the fourth mode has only about 2% of mass participation in the transversal (X) direction.

Fig. 17 Displacement components selected to compare the experimental and post-diction results
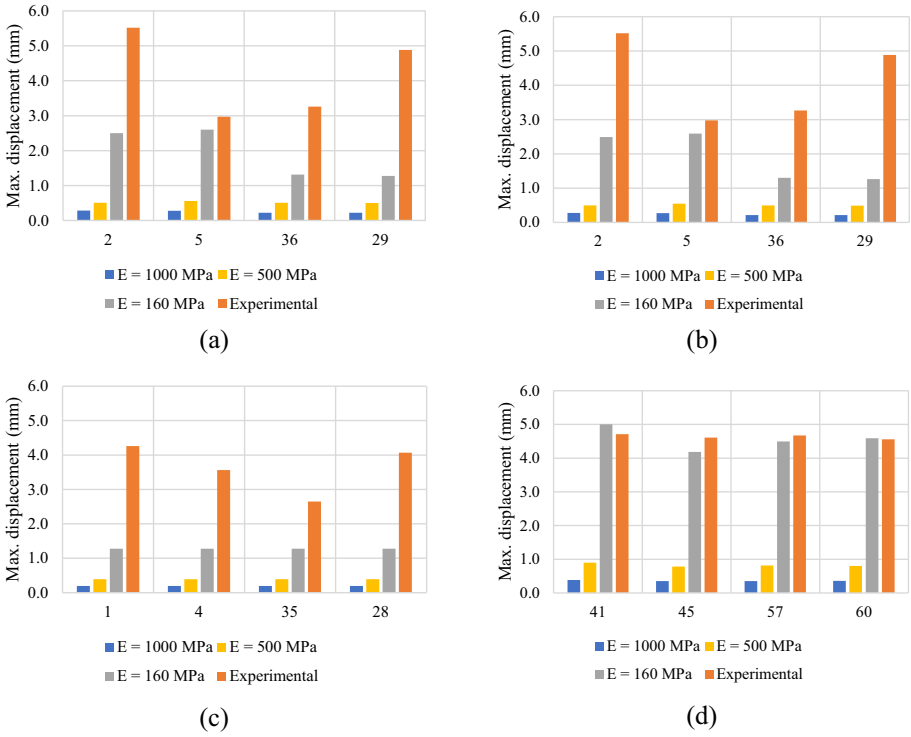
Fig. 18 Sensitivity analysis for different values of the Young's modulus of masonry: Unit 1 in the **a** X-direction, and **b** Y-direction; Unit 2 in the **c** X-direction, and **d** Y-direction

Table 6 Modal properties of the numerical model

Mode	Frequency (Hz)	T (s)	Mass participation (%)		
			MX	MY	MZ
1	5.7	0.18	40.70	0.00	0.00
2	6.3	0.16	0.00	60.85	0.02
3	7.3	0.14	27.87	0.00	0.02
4	9.7	0.10	2.27	0.00	0.02

4.3.2 Damping ratio

As it was previously mentioned, a sensitivity analysis was carried out for the post-diction model with different damping ratios, namely 3% and 5%, as shown in Fig. 20. The analysis was performed for Run 1.3, and displacements were compared for each control point at Unit 1 and Unit 2. It is observed that as the damping ratio increases, the maximum displacement obtained at the control nodes decreases. Although most control points do not show significant changes, displacements at Unit 2 in the Y-direction with 5% damping are generally lower than the experimental values (16% less on average). The updated numerical model is aimed to have not a stiffer but a more ductile
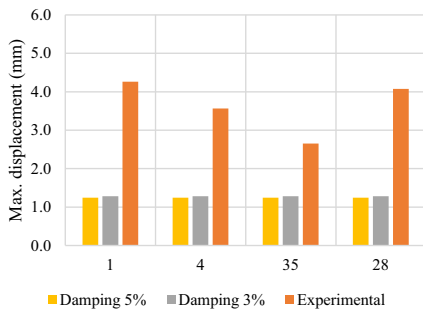
Fig. 19 First four mode shapes of the calibrated numerical model

Mode 1, $T = 0.18$ s

Mode 2, $T = 0.16$ s
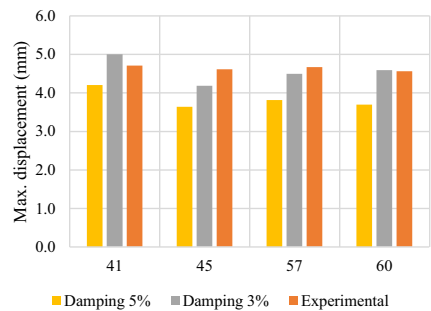
Mode 3, $T = 0.14$ s

Mode 4, $T = 0.10$ s
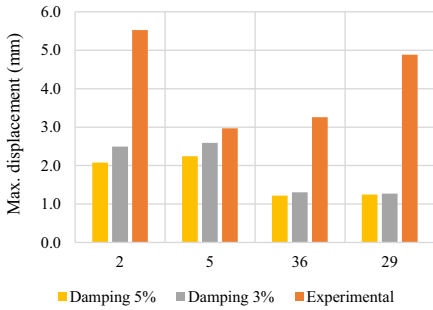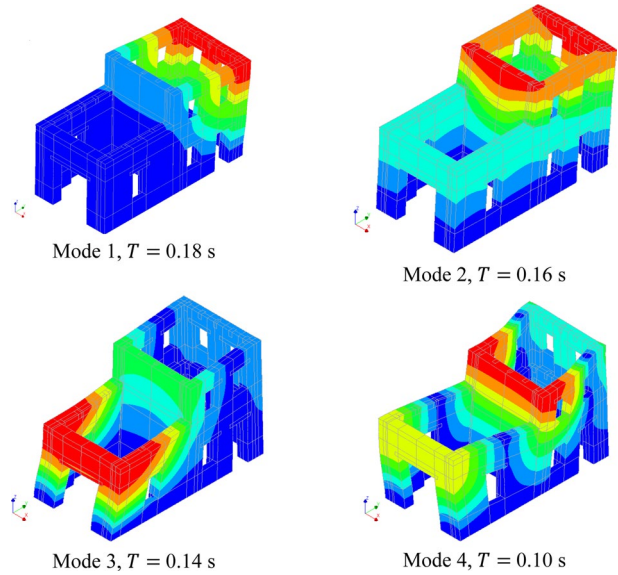
(a)
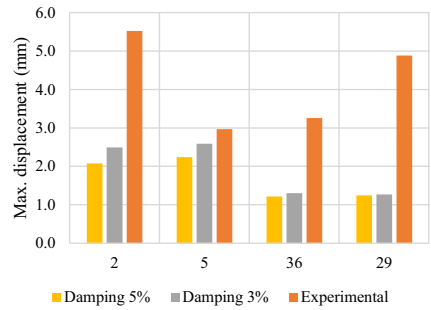
(b)

(c)

(d)

Fig. 20 Sensitivity analysis for different values of the damping ratio: Unit 1 in the **a** X-direction, and **b** Y-direction; Unit 2 in the **c** X-direction, and **d** Y-direction
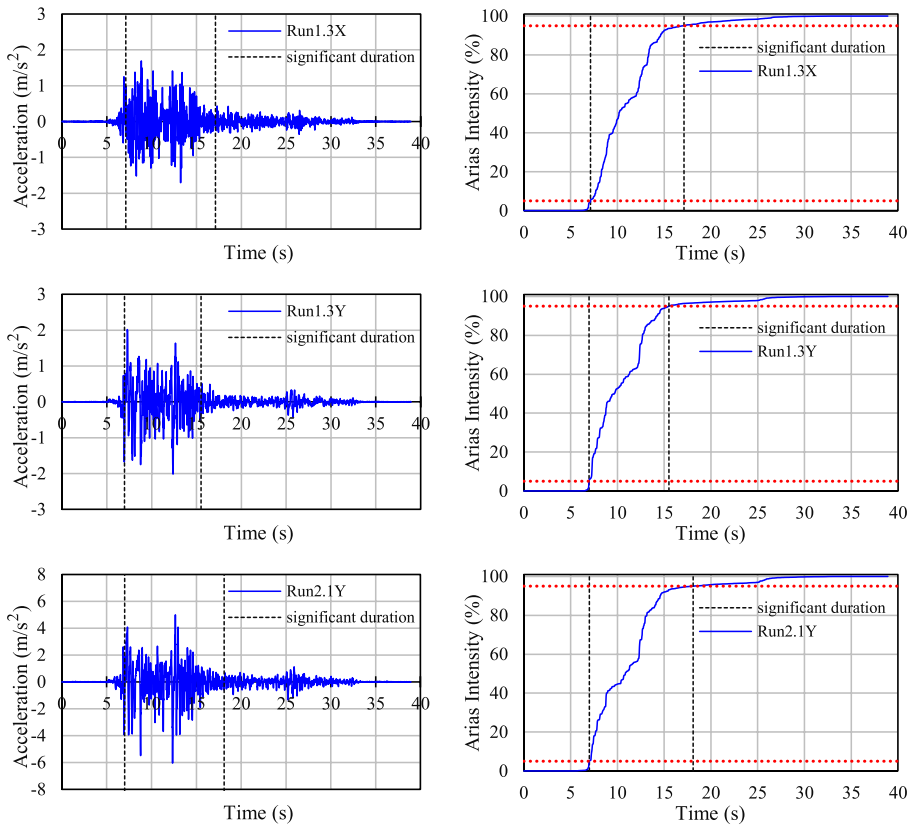
Fig. 21 Arias intensity and significant duration of the input Run 1.3 and Run 2.1

behaviour. Therefore, a damping ratio of 3% is selected since it leads to results closer to the experimental data.

4.4 Post-processing of the dynamic input and consideration of significant duration

Non-linear time-history analyses require a high computational effort in DIANA. Thus, only a part of the strong ground motion was considered in this study to speed up the process. The duration of each record was shortened by considering a significant portion obtained according to the accumulation of energy in the accelerogram, namely Arias intensity. In this sense, the significant duration represents an interval by taking into account the characteristics of the entire accelerogram and defining the strong part of the motion that might influence most of the seismic response. In the present study, the significant duration is obtained based on the time frame between 5 and 95% of Arias intensity (Trifunac and Brady 1975). Figure 21 depicts, for each dynamic input studied, the cumulative energy curve of the Arias intensity and their significant durations. It is found that the significant duration for Run 1.3 X-component, Run 1.3 Y-component, and Run 2.1 Y-component are 10.00 s, 8.54 s, and 11.10 s, respectively. The duration of the shortened input is decided to be 15.00 s to cover the significant portions for each component.
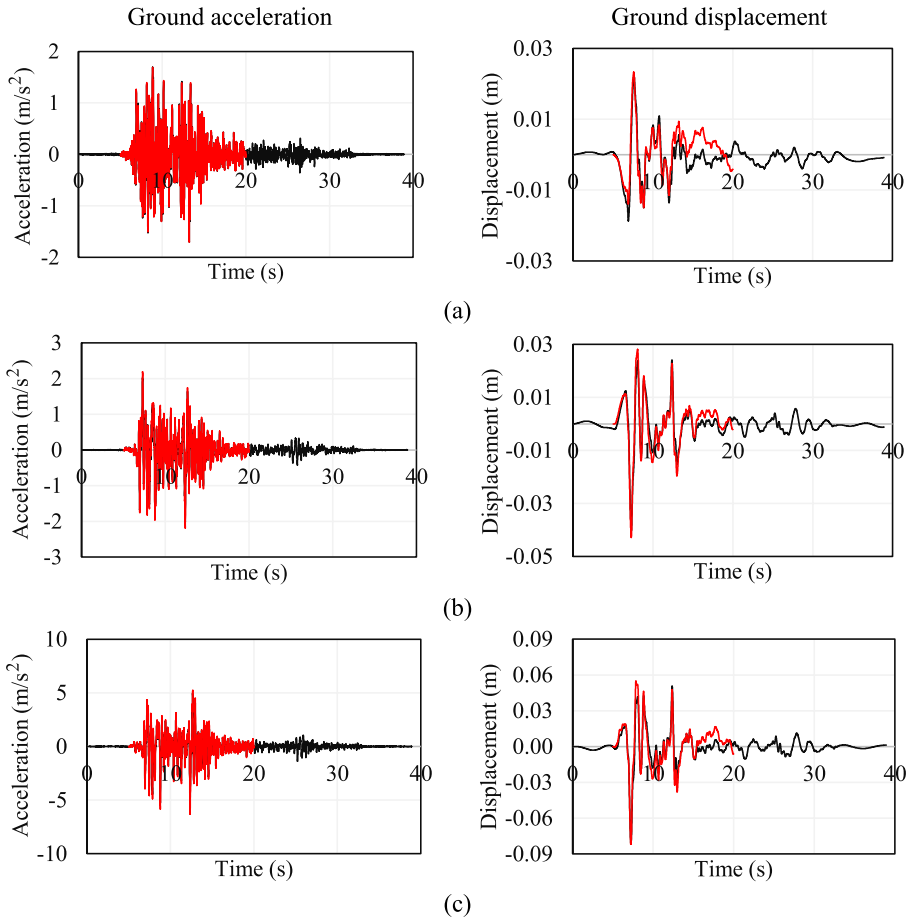
Fig. 22 Time series of ground acceleration and displacement for: **a** Run 1.3 in the X-direction; **b** Run 1.3 in the Y-direction; **c** Run 2.1 in the Y-direction. (Black represents the complete input, and red represents the shortened input

Nevertheless, the shortened input needs to be processed to provide reliable results. When a complete seismic input is cropped by considering a certain time frame, it requires to be treated in time and frequency domains. This is mainly important for the displacement history of the input due to the double integration procedure of the accelerogram. In this regard, baseline correction and filtering were applied to the shortened input to provide a displacement history that coincides with the real earthquake input, as shown in Fig. 22. The authors are aware of the fact that once an accelerogram is treated by filtering and baseline corrections, the record itself differs from the original. Nonetheless, by providing the closest response for the displacement history of the input, such an approach is considered expedient.

4.5 Post-diction results: comparison and discussion

Considering the improvements implemented in the updated model, post-diction analyses were performed, and the results are discussed in the present section. As mentioned in the methodology, only two dynamic inputs were applied, namely, Run 1.3 and Run 2.1. The comparison between experimental and post-diction results was done in terms of displacements at selected nodes (Fig. 17), principal tensile strain distribution, and base shear force.

4.5.1 Results at the end of run 1.3

Experimental displacements were analysed to have insight into the response of the aggregate building. As it was previously noted, there was no evidence of out-of-plane cracks at the early stages of the damage accumulation. In this sense, the displacements at the top level of Unit 2 were investigated to understand if the unit was dominated by local (out-of-plane) or global (in-plane) behaviour. Therefore, the displacement components that were located in the out-of-plane and in-plane direction (considering the longitudinal seismic input) were considered, namely Node 41, Node 46, and Node 57. The Incremental Dynamic Analysis (IDA) curve of these nodes concerning each dynamic input illustrates that the displacement values of these three nodes are almost the same up to Run 1.3 in which no damage to the structural walls was observed. This indeed depicts a global response meaning that the displacements in the in-plane and out-of-plane walls do not have a considerable difference, as presented in Fig. 23.

The numerical validation within the linear range of the post-diction model was performed based on Run 1.3 by comparing the displacement values of the same control points at the roof level of Unit 2. Figure 24 presents the experimental and numerical displacement time histories of the studied nodes. It is observed that the trend of the dynamic input differs, which is expected due to the consideration of significant duration and filtering. Nevertheless, the peak displacement values for each node at Unit 2 are reasonably accurate
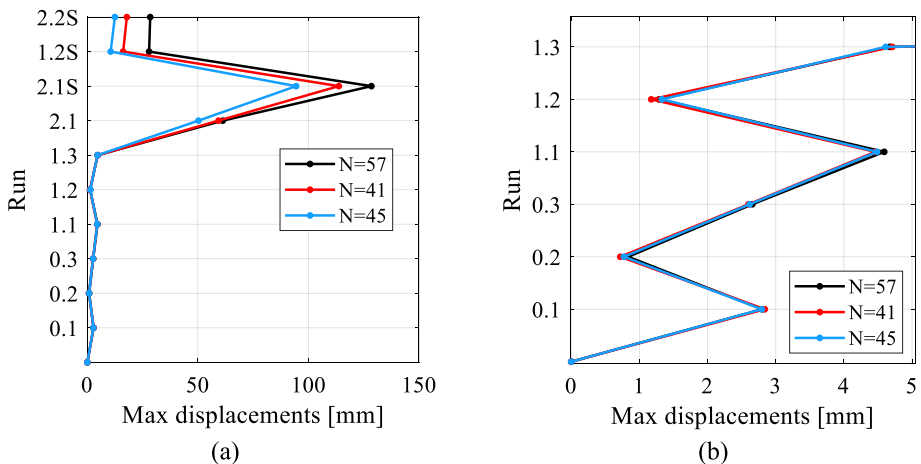

Fig. 23 Plot of the Incremental Dynamic Analysis of selected displacements components: **a** for all runs; **b** zoom-in of the elastic range (adapted from Tomić et al. (2022))
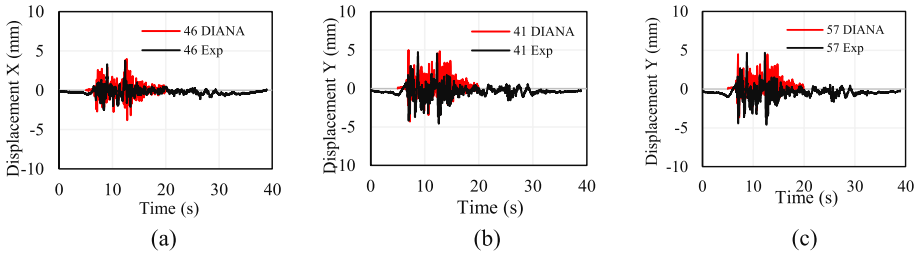
Fig. 24 Comparison of the experimental and numerical displacement histories of selected nodes at Unit 2, for Run 1.3: **a** Node 46; **b** Node 41; **c** Node 57

and within the experimental range. As was mentioned, the top level of Unit 2 appears to be governed by the global response in the longitudinal direction.

As shown in Fig. 25, at the end of Run 1.3 there is a strain concentration in Unit 2 which was not observed in the experimental campaign. The authors believe that these strain concentrations occur since no improvements were introduced in the transversal direction, e.g., the tying of the two parallel walls (Façade 2 and Façade 3). Furthermore, DIANA considers a 'scan' output command to plot the cumulative strain distribution. This command assumes the maximum and least favourable scenarios for each time step and adds up the results continuously throughout the analysis, which may lead to an overestimation of the recorded crack distribution.

The comparison of the experimental and numerical base shear force-time histories is presented in Fig. 26, for Run 1.3 (X- and Y-component). The graphs point out a good correspondence between numerical and experimental results. As for the maximum registered values, the base shear value obtained for Run 1.3 along the X-direction is equal to 42 kN and the corresponding experimental value is about 55 kN. Better results are achieved in the case of Run 1.3 along the Y-direction, with a numerical value of 54 kN and an error of 8%.

Although the updated modulus of elasticity is unrealistically low, the simulated displacements in Unit 1 are still lower than the experimental values for both the X- and Y-direction regardless of seismic intensity (Fig. 27a, b). The differences range from 12 to 74% at the control points of Unit 1 in the X-direction, whereas the lowest difference in Unit 2 is 7% and the highest one is 80%. Moreover, the behaviour of Unit 1 seems to be asymmetric, for instance, displacement components 2 and 5 at Façade 1 have different levels of displacement in the transversal (X) direction and a similar response is registered for displacement components 29 and 36 next to the interface. On the other hand, the post-diction

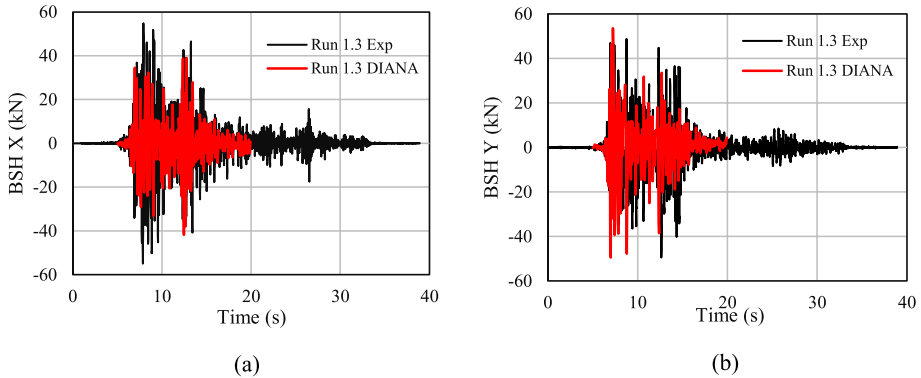**Fig. 25** Principal tensile strain distribution at the end of Run 1.3
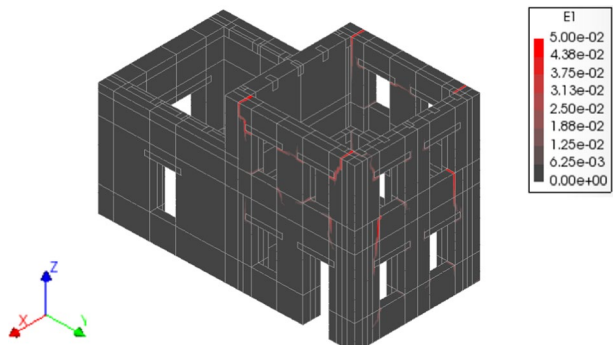
Fig. 26 Comparison of the experimental and numerical base shear force–time histories: **a** Run 1.3X; **b** Run 1.3Y

model shows a similar level of deformations for each façade in the transversal (X) direction. This behaviour resembles the vibration mode shape 3 (Fig. 19), which is characterized by a more prominent transversal movement of Façade 1.

Considering the longitudinal (Y) direction in Unit 1, the updated simulation does not reach the level of deformation registered during the test, and there is a considerable difference in the maximum displacements registered for the displacement components, with an average error of 64% (Fig. 27c). Note that the displacements obtained in the numerical model have the same value due to the tying elements imposed at the roof level of Unit 1.

In the case of Unit 2, the simulation reveals asymmetric displacements in the X-direction, with greater movements of Façade 4 and significantly lower displacements at Façade 5 (Fig. 27b). Conversely, the experimental values are almost the same for all the control points and the maximum difference is almost 9%. On the other hand, the agreement between experimental and simulated maximum displacements is noticeable for the longitudinal (Y) direction. The imposed tying system ensured a uniform movement similar to the one perceived during the test (Fig. 27d).

According to these results, a set of tying elements might be needed to improve Unit 2 in the X-direction as well. It must be noted, however, that the response of Unit 2 in the transversal direction might be further influenced by the interface, which needs to be adjusted by taking these results into account.

4.5.2 Results at the end of run 2.1

The comparison of the experimental and numerical base shear force–time histories is presented for Run 2.1 (X- and Y- components) in Fig. 28. Considering the X-component of Run 2.1, the experimental shear values are slightly higher with respect to the achieved numerical values. On the other hand, a good correspondence is obtained for Run 2.1 along the Y-direction, apart from the experimental peak value (162 kN); in this case, the maximum registered numerical value was 112 kN.

Unit 1 shows Y-displacements with a similar trend as the ones registered for the previous signal (Run 1.3), but on this occasion with greater values, as expected. The imposed tying elements at the roof level prevent the development of the experimentally observed behaviour, which in turn reveals a significant variation of maximum displacements
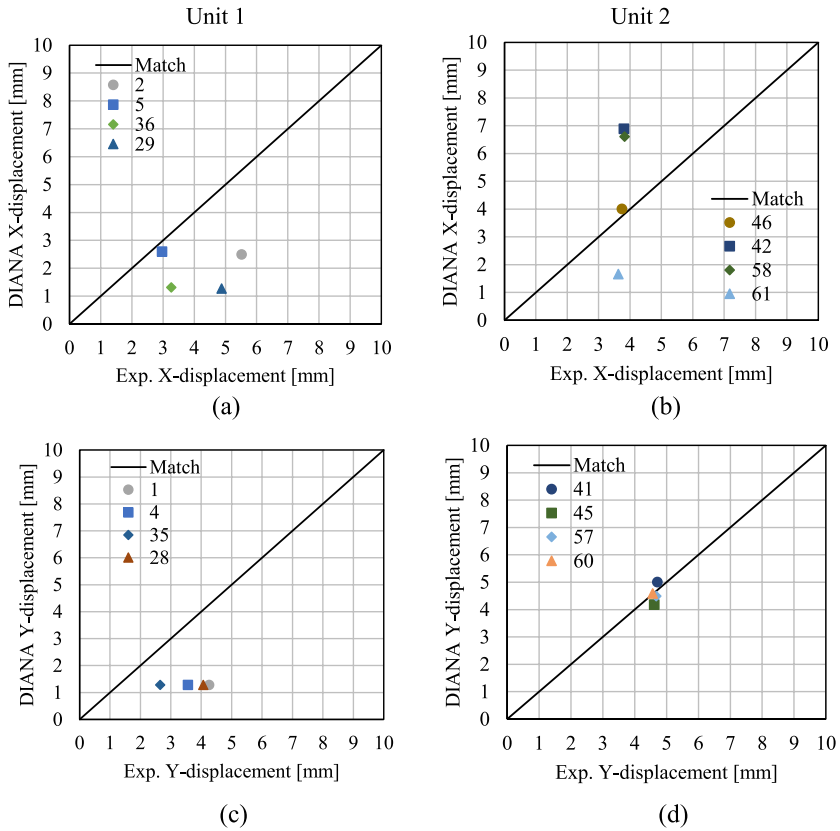
Fig. 27 Comparison of the maximum experimental and numerical displacements for Run 1.3 for (**a** Unit 1, X-direction; **b** Unit 2, X-direction; **c** Unit 1, Y-direction; **d** Unit 2, Y-direction

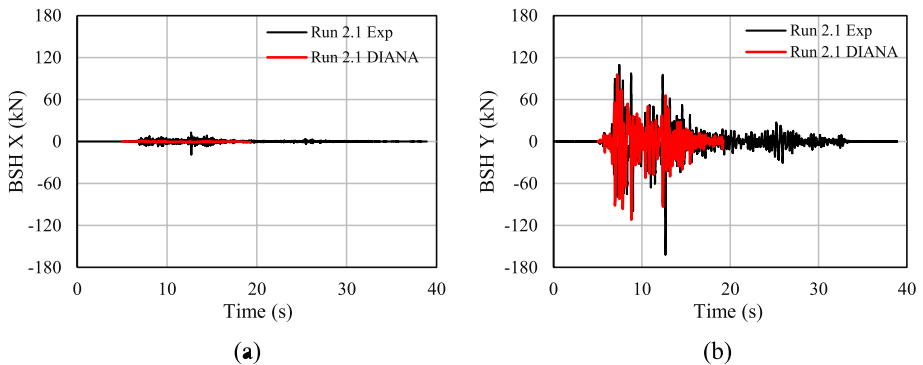and points out an asymmetric behaviour (Fig. 29). In the case of Unit 2, there is a good

Fig. 28 Comparison of the experimental and numerical base shear force–time histories: **a** Run 2.1X; **b** Run 2.1Y
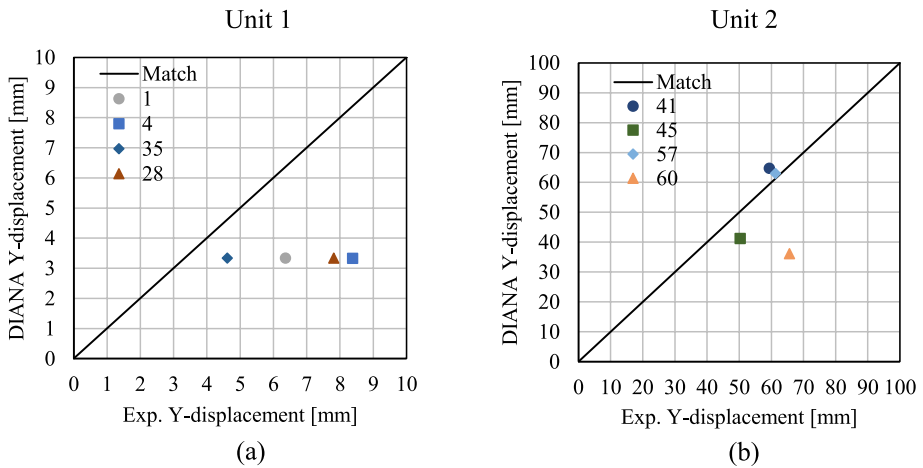
Fig. 29 Comparison of the maximum experimental and numerical displacements for Run 2.1 for **a** Unit 1, Y-direction; **b** Unit 2, Y-direction
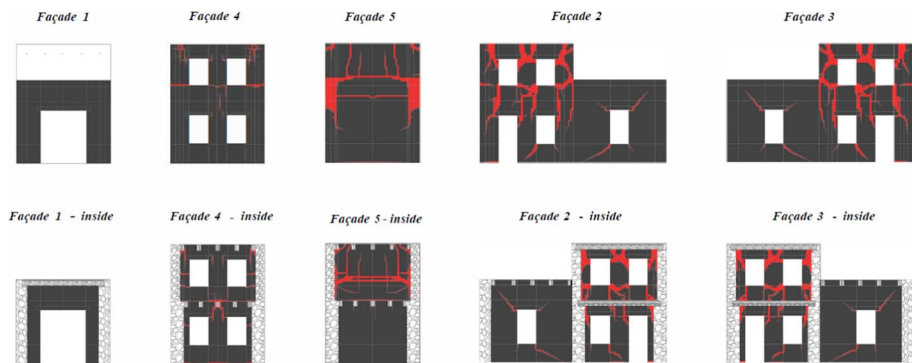

Fig. 30 Principal tensile strain distribution at the end of Run 2.1

agreement between the experimental and numerical results obtained for Run 2.1 with differences ranging between 3 and 18%. Nevertheless, the maximum displacement reached by the post-diction model for Façade 5 (displacement component 60) is 45% lower, which might be caused by the influence of the interface or the development of damage in that area. Overall, the behaviour seems to be well-captured by the simulation.

Finally, post-diction and experimental results are qualitatively compared in terms of damage mechanisms, with reference to Run 2.1. Figure 30 shows the crack map obtained from the FE model. For the experimental damage map, the reader is referred to Fig. 8. Regarding Unit 2, the comparison points out a good replication of the damage mechanism for Façade 2 and Façade 3, characterized by the presence of flexural cracks, as already observed in the pre-diction phase. The damage mechanism of Façade 4 is also well replicated, showing the presence of flexural and horizontal out-of-plane cracks, which were not recorded in the pre-diction analysis. An improvement is registered in the correspondence between numerical and experimental results regarding Façade 5, which now replicates the

experimental horizontal crack registered at the roof level of Unit 1. On the other hand, the façade shows flexural cracks at the second storey which were not recorded experimentally, and a strain concentration at the interface between the two units, probably due to a too-stiff behaviour in that area. Additionally, the experimental model presents a horizontal crack at the bottom, not reproduced by the FE model. Considering Unit 1, no cracks were recorded in Façade 1, for both the numerical and the test models. On the other hand, Façades 2 and 3 are characterized by shear cracks which were not recorded experimentally. These cracks are probably caused by the introduction of the tying links at the roof level, which imposed a uniform displacement and forced the longitudinal walls to behave in the in-plane.

5 Conclusions

This work presents a series of numerical simulations carried out on a three-dimensional continuum finite element model representing a two-unit stone masonry aggregate subjected to horizontal dynamic excitation. The work was developed within the framework of the SERA—AIMS project and involved two distinct stages, namely a blind pre-diction and a post-diction phase. In the first step, the numerical model was developed based on pre-test information and literature data. Then, based on the actual seismic input and experimental data, the initial model was updated, and post-diction analyses were performed. The accuracy of the numerical models was analysed in terms of base shear force, maximum displacements, and damage patterns.

This final section summarizes the main outcomes of the present study and provides several recommendations on strategies to be implemented in blind prediction and post-diction analyses.

Outcomes:

- In the present research, a finite element continuum model was prepared using a macro-modelling approach. The presented approach was able to qualitatively predict the damage with reasonable accuracy.
- The experimental response of the structure was studied, and it was observed that the response is mainly governed by global behaviour, whereas no signs of localized failure mechanisms were observed at the early stage of the testing campaign. The blind prediction model showed local out-of-plane damage which was not developed in the actual test. Therefore, the modelling assumptions were updated considering this aspect to ensure a more global response for the post-diction model.
- As a starting point, the material properties provided by the experimental campaign were considered in the pre-diction simulations. The numerical model was found to be particularly stiff with the Young's modulus of 3.4 GPa for masonry. Although the Young's modulus of the pre-diction model was reduced by 40% to adopt the lower bound limit according to the Italian Code, the predicted displacements were significantly lower than the experimental ones, nearly 90% less.
- Based on the comparison of the blind-prediction model with experimental results, a set of upgrades was considered to improve the numerical simulation: (a) introduction of non-linear interface elements to simulate the contact between Unit 1 and Unit 2; (b) introduction of tying elements in the windows and at the roof level of each unit; (c) calibration of the elastic modulus.

- Disconnecting the two aggregate units in the FE model prevented any interaction between the adjacent structures. For the updated model, nonlinear interface elements were assigned to reproduce the pounding effect and contribute to the transfer of forces between the units.

- Tying elements in place of the floor timber beams were able to reproduce a more effective box-type behaviour.

- Two runs of the experimental campaign were chosen to calibrate the initial model and improve its behaviour. The last run before the appearance of extensive damage (Run 1.3 with X- and Y-component) was used to update the linear elastic properties, namely the elastic modulus, whereas the run where most cracks developed (Run 2.1 in Y-direction) was used to model the damage pattern. For the calibration of the linear stiffness, choosing the Young's modulus as the main parameter for calibration can lead to reasonably accurate results. However, for the present case, an unrealistic limit had to be reached to simulate the observed experimental behaviour (nearly 20 times less than the value obtained in the material characterization tests). Other strategies could be suggested to calibrate the linear stiffness of the structure, such as the introduction of nonlinear interfaces at the base.

- The two signals were run in parallel as two independent analyses, namely Run 1.3 and Run 2.1. Due to the high computational cost required to simulate each sequence, only the significant duration of the original signal was considered. The displacement history of the original record was considered as a reference and baseline correction was carried out to avoid unreliable input.

- Considering the post-diction results, the differences in the values of the base shear force for the simulated and experimental results were 8% and 30% for Run 1.3 and Run 2.1, respectively.

- The maximum displacements for Unit 1 obtained with the updated model were still lower than the experimental values (up to 74%) despite the low elastic modulus. The displacements obtained in the Y-direction were considerably improved after the updating of the elastic modulus and the introduction of tying elements. Nonetheless, the simulated behaviour of Unit 2 close to the interface (Façade 5) was still more rigid than the experimental one. The interaction with Unit 1 through the interface could be the cause for these dissimilarities. Thus, further tuning of the interface properties could be necessary to improve the simulated behaviour while keeping the interaction between the two aggregates. On the other hand, the numerical displacements obtained in the X-direction (Run 1.3) depict different dynamic trends with respect to the experimental behaviour. A secondary tying system in the transversal direction could improve the displacements for the X-component.

- Regarding damage patterns in the post-diction model, slight damage was registered at the end of Run 1.3, localised at the top of Unit 2, which might be linked to the transversal excitation. This damage was not developed during the test and could be related to the lack of connection between the longitudinal walls (Façade 2 and Façade 3), which was ensured for the other two walls by means of the tying elements. Since Run 2.1 was calculated independently, this damage was not considered of further relevance.

- The damage simulated during the updated Run 2.1 was mostly concentrated in the in-plane walls, which was a great improvement with respect to the pre-diction results. Slight damage developed in Unit 1, which was not registered experimentally. In this sense, the tying links implemented at the roof level could have induced these cracks by imposing a uniform displacement and forcing the longitudinal walls to respond in-plane. The damage pattern obtained for the transversal walls of Unit 2 (Façade 4 and Façade 5) is well-repli-

cated showing the presence of flexural and horizontal out-of-plane cracks, which were not recorded in the pre-diction analysis.

Recommendations:

- *Blind prediction stage* As a starting point, it is suggested that material properties provided by the experimental campaign be considered for the preliminary analysis. Yet, it is important to judge the results of the simulation. If necessary, changes to material properties could be applied based on the suggestions of codes or provisions. In the present case, the Young's modulus was considered too high and the experimental value was reduced (40%) according to the lower bound limit suggested by the Italian Code.
- *Post-diction stage* The first and most important step of the study is to process the provided experimental results in order to understand if the behaviour of the structure is local or global. This will help to define an approach to improve the numerical model and simulate a more consistent response. Secondly, it is important to choose an approach to calibrate the numerical model. The natural frequency can be selected as a target parameter if the dynamic properties of the structure are available. Otherwise, a response parameter should be selected, such as displacement at a control point (preferably within linear range). Finally, to achieve the target parameter, a variable (or set of variables) is needed, namely damping ratio, Young's modulus, interface properties (if applicable), and boundary conditions (if applicable). In this context, a sensitivity analysis can be performed to understand the impact of each variable on the overall numerical response. Consequently, the numerical model can be calibrated by tuning the selected variables until reaching the target parameter.

In general, the overall approach and proposed methodology seem to be expedient for the structural analysis of existing masonry aggregates. Nonetheless, the available data regarding real structures is still scarce and further studies should be performed to provide new input information and achieve a more consistent response of the numerical models. In the present study, the missing dynamic properties of the tested specimen would be a valuable input to support the calibration process.

Author contributions All authors contributed to the development of the work throughout its different phases, starting from the study conception, methodology and design. All authors were involved in the analysis and interpretation of results. The first draft of the manuscript was written by AA and JD; all authors commented on previous versions of the current manuscript. Finally, all authors read and approved the final manuscript.

Declarations

Conflict of interest The authors declare that they have no known competing financial interests or personal relationships that could have appeared to influence the work reported in this document.

References

Araújo AS (2014) Modelling of the seismic performance of connections and walls in ancient masonry buildings, PhD Thesis. University of Minho, Guimarães

ASCE 41/13 (2014) Seismic evaluation and retrofit of existing buildings. American Society of Civil Engineers

Aşıkoğlu A, Avşar Ö, Lourenço PB, Silva LC (2019) Effectiveness of seismic retrofitting of a historical masonry structure: Kütahya Kurşunlu Mosque, Turkey. Bull Earthq Eng 17:3365–3395. https://doi.org/10.1007/s10518-019-00603-6

Aşıkoğlu A, Vasconcelos G, Lourenço PB, Pantò B (2020) Pushover analysis of unreinforced irregular masonry buildings: Lessons from different modeling approaches. Eng Struct. https://doi.org/10.1016/j.engstruct.2020.110830

Aşıkoğlu A, Vasconcelos G, Lourenço PB (2021) Overview on the nonlinear static procedures and performance-based approach on modern unreinforced masonry buildings with structural irregularity. Buildings. https://doi.org/10.3390/buildings11040147

Bianchini N, Mendes N, Lourenço P (2020) Seismic evaluation of Bagan heritage site (Myanmar): the Loka-Hteik-Pan temple. Structures 24:905–921. https://doi.org/10.1016/j.istruc.2020.01.020

Bianchini N, Mendes N, Calderini C et al (2022) Seismic response of a small - scale masonry groin vault: experimental investigation by performing quasi - static and shake table tests. Bull Earthq Eng 20:1739–1765. https://doi.org/10.1007/s10518-021-01280-0

Carocci C, Tocci C, Cattari S, Lagomarsino S (2009) Linee Guida per gli interventi di miglioramento sismico degli edifici in aggregato nei centri storici

Cattari S, Frumento S, Lagomarsino S, Resemini S (2006) Multi-level procedure for the seismic vulnerability assessment of masonry buildings: The case of Sanremo (north-western italy). In: First European conference on earthquake engineering and seismology. Geneve

CEN (2009) UNI EN 338: structural timber — strength classes - British Standards Institute

Chopra AK (2012) Dynamics of structures theory and application to earthquake engineering, 4th edn. Printince Hall, New Jersey

Circolare NTC (2018) Circolare esplicativa delle norme tecniche per le costruzioni. Ministero delle Infrastrutture e Trasporti

De Sortis A, Di G, Dolce PM, et al (2009) Linee guida per la riduzione della vulnerabilità di elementi non strutturali arredi e impianti PRESIDENZA DEL CONSIGLIO DEI MINISTRI DIPARTIMENTO DELLA PROTEZIONE CIVILE Via Vitorchiano 4, Roma www.protezionecivile.it

DIANA FEA (2022) DIANA finite element analysis. DIANA FEA BV, Delft, The Netherlands

DPC (2012) Linee guida per modalità di indagine sulle strutture e sui terreni per i progetti di riparazione, miglioramento e ricostruzione di edifici inagibili. Napoli, Doppiavoce

DPCM (2011) Direttiva del Presidente del Consiglio dei Ministri del 9 febbraio 2011. Valutazione e riduzione del rischio sismico del patrimonio culturale con riferimento alle Norme tecniche per le costruzioni di cui al decreto del Ministero delle Infrastrutture e dei. Gazzetta Ufficiale della Repubblica Italiana n. 47 del 26 febbraio 2011, Supplemento Ordinario n. 54

Eurocode 8 (2005) Design of structures for earthquake resistancepart 3: assessment and retrofitting of buildings

Fragiadakis M, Vamvatsikos D (2010) Fast performance uncertainty estimation via pushover and approximate IDA. Earthq Eng Struct Dyn 39:683–703. https://doi.org/10.1002/eqe.965

Giuffré A (1990) Mechanics of historical masonry and strengthening criteria. In: Kappa E (ed) XV regional seminar on earthquake engineering. Edizioni Kappa Rome, Rome

Giuffrè A, Baggio C, Carocci C (1993) Sicurezza e conservazione dei centri storici: il caso Ortigia: codice di pratica per gli interventi antisismici nel centro storico. Laterza, Rome

Imai K, Frangopol DM (2000) Geometrically nonlinear finite element reliability analysis of structural systems. I: theory. Comput Struct 77:677–691. https://doi.org/10.1016/S0045-7949(00)00010-9

Liu Y, Kuang JS (2017) Spectrum-based pushover analysis for estimating seismic demand of tall buildings. Bull Earthq Eng 15:4193–4214. https://doi.org/10.1007/s10518-017-0132-8

Lombardo G, Greco A, Caddemi S, et al (2018) La vulnerabilità sismica degli edifici storici in aggregato. Nuove Metodol Negli Approcci Speditivi Model Strutt

Lourenço PB, Ramos LF (2004) Characterization of cyclic behavior of dry masonry joints. J Struct Eng. https://doi.org/10.1061/(ASCE)0733-9445(2004)130:5(779)

Lourenço PB, Avila L, Vasconcelos G et al (2013) Experimental investigation on the seismic performance of masonry buildings using shaking table testing. Bull Earthq Eng 11:1157–1190. https://doi.org/10.1007/s10518-012-9410-7

Lourenço PB (1996) Computational strategies for masonry structures. Delft University of Technology

Mendes N, Lourenço PB (2014) Sensitivity analysis of the seismic performance of ancient masonry buildings. Eng Struct 80:137–146. https://doi.org/10.1016/j.engstruct.2014.09.005

Mendes N (2012) Seismic assessment of ancient masonry buildings: Shaking table tests and numerical analysis. University of Minho

Mendes N (2014) Seismic assessment of ancient masonry buildings: shaking table tests and numerical analysis Universidade do Minho escola de engenharia nuno adriano leite mendes seismic assessment of ancient masonry buildings: shaking table tests and numerical analysis

MIBACT (2010) Linee guida per la valutazione e riduzione del rischio sismico del patrimonio culturale allineate alle nuove Norme tecniche per le costruzioni. Gangemi Editore spa, Rome

Milano L, Mannella A, Morisi C, Martinelli A (2006) Allegato alle linee guida per la riparazione e il rafforzamento di elementi strutturali, tamponature e partizioni

Mochi G, Predari G (2016) La vulnerabilita sismica degli aggregati edilizi by EdicomEdizioni. Gorizia

NTC (2018) Norme tecniche per le costruzioni. DM 17/1/2018. Gazz Uff della Repubb Ital

ReLuis (2010) Linee guida per modalità di indagine sulle strutture e sui terreni per i progetti di riparazione, miglioramento e ricostruzione di edifici inagibili. Rome

Rots JG (1988) Computational modeling of concrete fracture. PhD Thesis. Delft University of Technology

Senaldi I, Guerrini G, Scherini S, et al (2018) Natural stone masonry characterization for the shaking-table test of a scaled building specimen. In Proceedings of the 10th international masonry conference. pp.1530–1545

Tomić I, Penna A, Dejong MJ (2022) Shake table testing of a half-scale stone masonry building. Bull Earthq Eng 18:609–643

Trifunac MD, Brady AG (1975) A study on the duration of strong earthquake ground motion. Bull Seismol Soc Am 65:581–626

Zacharenaki AE, Fragiadakis M, Papadrakakis M (2013) Reliability-based optimum seismic design of structures using simplified performance estimation methods. Eng Struct 52:707–717. https://doi.org/10.1016/j.engstruct.2013.03.007